

SCHOLARLY COMMONS

Publications

8-13-2019

Comparison Between Fluid Simulation with Test Particles and 1 Hybrid Simulation for the Kelvin-Helmholtz Instability

Xuanye Ma

Embry-Riddle Aeronautical University, max@erau.edu

Katariina Nykyri

Embry-Riddle Aeronautical University, nykyrik@erau.edu

Brandon L. Burkholder

Embry-Riddle Aeronautical University, BURKHOLB@erau.edu

Rachel C. Rice

Embry-Riddle Aeronautical University, RICER4@my.erau.edu

Peter A. Delamere

University of Alaska

See next page for additional authors

Follow this and additional works at: https://commons.erau.edu/publication



Part of the Atmospheric Sciences Commons

Scholarly Commons Citation

Ma, X., Nykyri, K., Burkholder, B. L., Rice, R. C., Delamere, P. A., & Neupane, B. (2019). Comparison Between Fluid Simulation with Test Particles and 1 Hybrid Simulation for the Kelvin-Helmholtz Instability. Journal of Geophysical Research: Space Physics, (). https://doi.org/10.1029/2019JA026890

This Article is brought to you for free and open access by Scholarly Commons. It has been accepted for inclusion in Publications by an authorized administrator of Scholarly Commons. For more information, please contact commons@erau.edu.

Authors Xuanye Ma, Katariina Nykyri, Brandon L. Burkholder, Rachel C. Rice, Peter A. Delamere, and Bishwa Neupane	

Comparison between fluid simulation with test particles and hybrid simulation for the Kelvin-Helmholtz instability

- Xuanye Ma¹, Peter A. Delamere², Katariina Nykyri¹, Brandon Burkholder ^{1,2}, Bishwa

 Neupane ², Rachel C. Rice ¹
- Center for Space and Atmospheric Research, Embry-Riddle Aeronautical University, Daytona Beach, Florida, USA.
- ² Geophysical Institute, University of Alaska Fairbanks, Fairbanks, Alaska, USA.

Key Points:

- Kelvin-Helmholtz (KH) vortices in Hall MHD simulation can form large magnetic islands to transport plasma.
- Plasma mixing is mainly through diffusion in hybrid simulation of the KH instability.
 - Anisotropic temperature can be formed by the nonlinear KH instability, which can drive kinetic-scale waves.

Corresponding author: Xuanye Ma, max@erau.edu

Abstract

14

15

17

19

21

22

23

24

25

32

43

A quantitative investigation of plasma transport rate via the Kelvin-Helmholtz (KH) instability can improve our understanding of solar-wind-magnetosphere coupling processes. Simulation studies provide a broad range of transport rates by using different measurements based on different initial conditions and under different plasma descriptions, which makes cross literature comparison difficult. In this study, the KH instability under similar initial and boundary conditions (i.e., applicable to the Earth's magnetopause environment) is simulated by Hall MHD with test particles and hybrid simulations. Both simulations give similar particle mixing rates. However, plasma is mainly transported through a few big magnetic islands caused by KH driven reconnection in the fluid simulation, while magnetic islands in the hybrid simulation are small and patchy. Anisotropic temperature can be generated in the nonlinear stage of the KH instability, in which specific entropy and magnetic moment are not conserved. This can have an important consequence on the development of secondary processes within the KH instability as temperature asymmetry can provide free energy for wave growth. Thus, the double-adiabatic theory is not applicable and a more sophisticated equation of state is desired to resolve meso-scale process (e.g., KH instability) for a better understanding of the multi-scale coupling process.

1 Introduction

The Kelvin-Helmholtz (KH) instability, as one of the main mechanisms of viscouslike interaction between the solar wind and the planets' magnetosphere/ionosphere, has
been widely observed at various solar system objects for decades (see *Johnson et al.* [2014]
and their reference). Driven by the large sheared flow, it can operate under different interplanetary magnetic field (IMF) orientations [*Kavosi and Raeder*, 2015; *Henry et al.*, 2017].

It can be responsible for the transport of momentum and energy [*Miura*, 1984; *Pu and Kivelson*, 1983]. In addition, the KH instability can trigger secondary instabilities (e.g., reconnection and wave-particle interaction) in the nonlinear stage to break the frozen-in condition, which transports plasma, flux tube entropy, and magnetic flux [*Ohsawa et al.*, 1976; *Otto and Fairfield*, 2000; *Nykyri and Otto*, 2004; *Ma et al.*, 2014a,b; *Ma et al.*, 2017; *Delamere et al.*, 2011, 2018]. Furthermore, several nonadiabatic heating mechanisms are expected to be attributed to the KH instability and the associated secondary instability (e.g., [*Moore et al.*, 2016; *Masson and Nykyri*, 2018]).

50

55

63

70

71

72

73

Quantitative investigation of the transport processes in the KH instability as a macro scale diffusion process under different IMF conditions is critical to our understanding of the interaction between the solar wind and the Earth's magnetosphere. Simulation studies from magnetohydrodynamics (MHD) to particle-in-cell (PIC) simulation show a large range of transport rates from $10^9 \,\mathrm{m}^2 \,\mathrm{s}^{-1}$ to $10^{11} \,\mathrm{m}^2 \,\mathrm{s}^{-1}$ for Earth's magnetopause environments [Miura, 1984; Nykyri and Otto, 2001, 2004; Cowee et al., 2009, 2010; Delamere et al., 2011; Ma et al., 2017; Nakamura et al., 2017]. The difference among these studies is not only due to considering different physics, but also because of using different onset conditions, as well as using different methods to quantify the transport rate, which actually represent different transported quantities and even different transport processes. For instance, Miura [1984] estimated the anomalous viscosity (i.e., momentum and energy transport rates) based on Maxwell and Reynolds stresses in a high-plasma-beta region ($\beta \gg 1$) for a symmetric configuration. In contrast, Nykyri and Otto [2001, 2004] calculated the plasma entry rate (i.e., mass and flux transport rates) based on the total plasma in the reconnected magnetic island for an asymmetric configuration with a plasma beta value close to unity. Hybrid simulations [Cowee et al., 2009, 2010] used a mixing parameter determined by the number of particles in a given cell which originated on a given side of the boundary. This allows to evaluate the mixing rate of superdiffusion driven by the KH instability with no initial perturbation and low plasma beta ($\beta = 0.1$). The fully kinetic 3-D simulation with periodic boundary conditions along the third dimension showed that in the later nonlinear stage the KH vortices lead to a spectrum of secondary KH and Rayleigh-Taylor instabilities, giving a mixing velocity that is about one percent of the initial shear flow speed [Nakamura et al., 2013; Nakamura and Daughton, 2014]. As such, it is difficult to identify the relative importance between different physics (e.g., Hall physics and ion finite Larmor radius effects) and physical processes (e.g., reconnection and superdiffusion) in the KH instability by comparing various studies from the literature.

The motivation of this study is to understand how kinetic physics affects the KH instability transport processes by comparing a fluid simulation with test particle and hybrid simulation under the same KH onset condition. In principle, the KH onset condition and the growth rate are mainly determined by the shear flow speed with respect to the local fast mode speed (i.e., the sum of the Alfvén speed and acoustic speed), the magnetic field along the sheared flow direction, and the KH wavelength with respect to the width of initial sheared flow and other typical length scales (i.e., ion inertia length or ion Lar-

mor radius) [*Miura and Pritchett*, 1982]. The density, thermal pressure, and transverse magnetic field (i.e., the magnetic field perpendicular to the KH wave vector) affect the KH growth rate via the local fast mode speed. However, the density asymmetry affects the mass transport rate. As an extreme case, no net plasma mass is transported by KH driven reconnection for a symmetric density and magnetic field condition. Therefore, the transport rate by KH instability driven reconnection is measured by the area of a magnetic island rather than the mass in the magnetic island in this study (see next section). In contrast, the plasma mixing due to the finite Larmor radius, being largely determined by the thermal pressure and magnetic field, always exists even without magnetic reconnection. The detailed numerical model and measurement of transport rate are introduced in Section 2. The results, discussion and summary are presented in Sections 3, and 4, respectively.

2 Methods

87

90

101

102

103

104

105

106

2.1 Fluid and hybrid simulations

The KH instability in two-dimensional (2-D) geometries will be simulated by both fluid (i.e., Hall MHD) and hybrid simulation under similar initial and boundary conditions within the same simulation domain. The behavior of test particles introduced into the fluid simulation, which evolve in accordance with the electric and magnetic fields, is compared with particles in the hybrid simulation.

The fluid simulation uses a leap-frog scheme to numerically solve the full set of resistive Hall MHD equations [*Potter*, 1973; *Birn*, 1980; *Otto*, 2001; *Nykyri and Otto*, 2004], in which the electric field **E** is given by

$$\mathbf{E} = -\left(\mathbf{u} - \frac{\mathbf{j}}{en}\right) \times \mathbf{B} + \eta \mathbf{j}.$$

Here, **u** is the ion bulk velocity, **j** is the current density, and η is the resistivity. The collisionless plasma implies a zero resistivity, except in the reconnection diffusion region. Thus, a current-dependent resistivity model: $\eta = \eta_0 \sqrt{j^2 - j_c^2} H(j - j_c) + \eta_b$ is applied in the fluid simulation, where $\eta_0 = 0.05$, critical current density $j_c = 1.1$, H(x) is the Heaviside step function [Arfken, 1985], and a background resistivity $\eta_b = 0.01$. This resistivity model switches on a resistivity only if a critical current density is surpassed, and the maximum value of the resistivity is less than 0.0475 during the whole simulation time. Our previous studies [Nykyri and Otto, 2001, 2004; Ma et al., 2014a,b; Ma et al., 2017] demon-

strated that the overall dynamics of the KH instability are insensitive to the parameters of this resistivity model.

The hybrid code (i.e., kinetic ions and massless fluid electrons) was first proposed by *Harned* [1982], and the particular algorithms for our code were developed by *Swift* [1995, 1996] and [*Delamere et al.*, 1999; *Delamere*, 2009; *Delamere et al.*, 2018]. The code assumes quasineutrality, and is nonradiative. The Lorentz force equation is solved following the Boris method [*Boris*, 1970; *Birdsall and Langdon*, 1991]. The electric field and magnetic fields are calculated on a rectangular Yee lattice [*Yee*, 1966] that ensures an easy calculation of the curls of the fields and maintains a divergence-free magnetic field. The magnetic field equations are updated with a second-order, predictor-corrector method. A resistive term based on ion-electron collisions, $\nu(\mathbf{u}_e - \mathbf{u}_i)$, is included in the electron momentum equation:

$$\mathbf{E} = -\mathbf{u}_e \times \mathbf{B} - \nu (\mathbf{u}_e - \mathbf{u}_i),$$

where ion and electron bulk velocities are \mathbf{u}_i and \mathbf{u}_e , respectively. The collision frequency, $\nu = 2 \times 10^{-4} \omega_g$, is set to alter the amount of diffusion in the hybrid code to ensure numerical stability, where ω_g is the ion gyrofrequency. The electron pressure term is not considered in this study.

All simulations are carried out in a rectangular domain $|x| \leq L_x = 20L_0$, $|y| \leq L_y = 15L_0$, where $L_0 = c/\omega_{pi} = 139\,\mathrm{km}$ is the ion inertia length. Here the x direction is the normal direction outward from the magnetosphere (MSP, x < 0) to the magnetosheath (MSH, x > 0); the z direction points to the North; and the y direction is mostly along the sheared flow direction based on the right-hand rule. Both fluid and hybrid simulation have a uniform grid resolution of $0.1L_0$ in all directions. The y boundary conditions are periodic. The x boundary is open with $\partial_x = 0$. The dimensions of the simulation domain are sufficiently large that all conclusions drawn in this study are insensitive to a larger simulation size along the x direction.

The initial steady state condition is a one dimensional tangential discontinuity layer, in which number density, $n=0.4\,\mathrm{cm^{-3}}$, thermal pressure, $p=\beta B_0^2/(2\mu_0)$, magnetic field $B_y=B_0\sin\theta$ and $B_z=B_0\cos\theta$ components are constant across the velocity shear, $u_y=u_0\tanh(x/L_0)$. Here, the magnetic field $B_0=50\,\mathrm{nT}$, the magnetic field tilt angle $\theta=5^\circ$, sheared flow velocity $u_0=0.5v_A$, the Alfvén speed $v_A=B_0/\sqrt{\mu_0n_0m_0}=172\,\mathrm{km\,s^{-1}}$, with vacuum permeability, μ_0 , and ion mass, m_0 . The plasma beta, β is set to 0.25. The

fast mode speed at the boundary is $v_f = \sqrt{c_s^2 + v_A^2} = \sqrt{\gamma \beta/2 + 1} v_A \approx 1.1 v_A$, and the fast mode Mach number $u_0/v_f = 0.45$. The Alfvén speed along the shear flow direction is $v_{A\parallel} = \sin\theta v_A \approx 0.09 v_A$, and the associated Mach number $u_0/v_{A\parallel} = 5.7$.

In principle, hybrid simulations for the KH instability can be self-seeded, resulting in initial small-scale KH waves that inversely cascade to larger scales at the later stage [Delamere et al., 2018]. The small-scale KH waves can diffuse the boundary layer, which affects the longest wavelength with respect to the initial width of the sheared flow. Hence, both fluid and hybrid simulations are triggered by a velocity perturbation in this study, which is given by $\delta \mathbf{u} = \delta u \nabla \Phi(x, y) \times \mathbf{e}_z$, where the stream function is $\Phi(x, y) = -\cos(k_y y) \cosh^{-2}(\frac{x}{2L_0})$, and the KH wave number along the y direction is $k_y = \pi/L_y$. The amplitude of the perturbation, δv , is slightly different in the hybrid and fluid simulation for a convenient comparison, which will be explained in more detail in Section 3.

This study only allows a single KH wave mode to operate in the simulation system, which serves the purpose of comparison between Hall MHD with test particle and hybrid simulations. The pairing process in a larger simulation box is often observed in numerical experiments (e.g., [Faganello et al., 2009; Cowee et al., 2009, 2010]). It is suggested that the pairing process increases the anomalous viscosity [Miura, 1997]. In contrast, MHD simulations with dimensions that allow the pairing process [Nykyri et al., 2017] showed that the overall mass transport rate is comparable to the results without the pairing process in a much smaller simulation box [Nykyri and Otto, 2001, 2004]. This result also agrees with the hybrid simulation results that a typical diffusion coefficient for KH instability with the pairing process is about 10×10^8 m² s⁻¹ to 10×10^9 m² s⁻¹, and this value decreases with more density asymmetry [Cowee et al., 2009, 2010].

2.2 Measurement of plasma mixing and reconnected area

The growth of KH instability is measured by the range of bulk velocity u_x component [Nykyri and Otto, 2004; Ma et al., 2014a]. The momentum transport rate (anomalous viscosity), v_{ano} is given by

$$v_{\rm ano} = \frac{\overline{T_{xy}^M} + \overline{T_{xy}^R}}{\rho d\overline{u_y'}/dx},$$

where, $T_{xy}^{M} = B_{x}B_{y}\mu_{0}^{-1}$ and $T_{xy}^{R} = -\rho u_{x}u_{y}'$ are the xy component of Maxwell and Reynolds stress, respectively, u_{y}' is the bulk velocity u_{y} component in the magnetospheric frame (i.e., x < 0 region), and the overline indicates the spatial average of the quantity T_{xy}^{M} , T_{xy}^{R} ,

and u'_y over one wave period [Miura, 1984]. This measurement can be directly applied to both fluid and hybrid simulation.

165

166

168

169

170

172

173

17/

175

176

177

179

181

183

184

186

188

190

192

193

10/

195

196

197

Magnetic islands can be generated via magnetic reconnection driven by 2-D nonlinear KH modes [Nykyri and Otto, 2001, 2004]. Integrating the density over the area of the detached magnetic islands is used to estimate the mass entry velocity (in units km s⁻¹) from the magnetosheath into the magnetosphere, and the diffusion coefficient (in units m² s⁻¹) with an additional assumption of 1000 km wide boundary layer [Nykyri and Otto, 2001, 2004]. The identification of the magnetic island transport direction is based on the density inside of the magnetic island, which requires initially different density across the sheared flow. This method has only been applied to the configuration where magnetic field components along the KH wave vector direction keep the same direction across the boundary, which is referred to as "type-II" reconnection by Nakamura et al. [2006]. In this case, the newly reconnected magnetic field line is still connected to the same side of shear flow boundary (i.e., magnetosheath to magnetosheath or magnetosphere to magnetosphere). In contrast, the "type-I" reconnection operates when magnetic field components along the KH wave vector direction are antiparallel across the boundary, which connects magnetic field lines from both the magnetosheath and magnetospheric sides [Nakamura et al., 2006; Nykyri et al., 2006]. As such, the reconnected magnetic island mixes the plasma from both sides.

It appears that the plasma transport and mixing by "type-I" and "type-II" reconnection, which is largely determined by the KH wave vector direction, are fundamentally different. In reality, the KH wave vector is mainly along the most unstable direction. As such, the type of reconnection can be very sensitive for the quasi-transverse magnetic field case, suggesting the singularity of the strict transverse magnetic field case. However, such singularity is caused by 2-D geometry, which does not exist in 3-D geometry. In 3-D geometry (non-periodic boundary condition along the third dimension), the localized nonlinear KH wave can cause a pair of reconnection sites away from the equatorial plane, which exchanges a portion of magnetosheath and magnetospheric flux tube and consequently transports plasma [*Otto*, 2006]. This process is called "double mid-latitude reconnection" [*Faganello et al.*, 2012; *Borgogno et al.*, 2015]. Note that this process does not provide a net mass transport in a symmetric configuration. *Ma et al.* [2017] estimated the mass transport rate with asymmetric density by identifying double-reconnected flux though fluid parcel and magnetic field line tracing, and found the mass transport rate can reach

 10^{10} m² s⁻¹. However, the presence of a flow-aligned magnetic field component (either "type-I" and "type-II") breaks the north-south asymmetry, which reduces the transport rate [*Ma et al.*, 2017].

199

201

202

203

205

206

207

208

209

210

212

214

215

216

217

218

219

221

223

224

225

226

227

228

229

230

The KH instability diffusion coefficient is also measured by particle mixed area in hybrid and PIC simulations, where a mixed cell is defined as one containing both ion species where the density of each species in the cell must be at least 25% of its initial nominal density [Cowee et al., 2009, 2010; Delamere et al., 2018]. Although the value of 25% is arbitrary, the overall result is insensitive to this value. Note that plasma mixing can be caused by magnetic reconnection, especially for "type-I" reconnection, it can also operate simply due to ion finite Larmor radius effects [Cowee et al., 2009]. For numerical computation, a value p=1 or 0 is assigned to a particle, if the initial position x of this particle is x=10 or x=10. For a given point x=11 means in this area indicates the mixing rate of this area, in which x=12 or 1 means no mixing, and x=13 means fully mixed. For a better visualization, the mixing rate is redefined as x=14 and x=15 means no mixing, and x=16 means no mixing, and x=17 means no mixing, and x=18 means no mixing, and x=19 means no mixing, and

For fluid simulations, test particles are introduced to estimate the mixing rate. In order to compare with the hybrid simulation results, a Maxwellian distribution of 100 particles per each 0.1×0.1 grid cell is initialized. The Maxwellian is based on the velocity, temperature, and density in the vicinity of the cell. The test particles are introduced only for |x| < 15, because trajectories of the particles outside of this region are dominated by the $\mathbf{E} \times \mathbf{B}$ drift. The charged particles are traced by solving the Lorentz equation of motion using the Boris [1970] method, which has been used to investigate high-energy particles in the cusp diamagnetic cavity [Nykyri et al., 2012]. The instantaneous values of the fields are determined by interpolating in time between snapshots of the fluid simulation results spaced one Alfvén time apart (i.e., $\tau_A = L_0/v_A \approx 0.81\,\mathrm{s}$). Note the parallel electric can efficiently accelerated the charge particle, which is often exaggerated by the resistivity model in the fluid simulation. Thus, the electric field in the test particle excludes the η **j** term. We interpreted magnetic **B** and $\left(\mathbf{u} - \frac{\mathbf{j}}{en}\right)$ at particles' positions first, and then applied the cross product to obtain the electric field, which avoids the parallel electric field from the numerical interpretation. The symmetric treatment of the time derivative in the Boris method maintains the temporal reversibility of the Lorentz equation. As such, this

code can trace back the test particles to reconstruct particle distributions based on Liouville's theory [Birn et al., 1997, 1998].

3 Results

231

232

233

235

237

239

240

241

242

243

244

246

248

249

250

251

252

253

255

257

258

259

260

261

262

Figure 1 shows the velocity u_x component (panel A), the anomalous viscosity, v_{ano} (panel B), the area of magnetic island, A_r (panel C), and the area of mixed region, A_M (panel D), as functions of the time from top to bottom, respectively, which roughly represents the overall dynamic properties of the fluid with test particle simulation (blue lines) and the hybrid simulation (red crosses). The yellow, green, and cyan background indicate the linear stage ($t \le 75$), the early nonlinear stage ($75 \le t \le 150$), and the later nonlinear stage (t > 150). The separation between early and later nonlinear stage at t = 150is because the mixing area from fluid with test particle appears different from the result from hybrid simulation, suggesting small scale physical processes missing from the fluid simulation may begin to play a role. The velocity normal component (i.e., u_x) is used to represent the growth of the KH instability, which is almost identical between the fluid and hybrid simulations after t = 20. The fluid system has a slightly faster growth rate than the hybrid system. The different KH growth rate between fluid simulation and kinetic simulation has been discussed by Nakamura et al. [2010] and Henri et al. [2013]. They noted that the typical MHD initial configuration for KH instability is not a kinetic equilibrium. The initial relaxing process leads to a quick enlargement of the original shear layer in PIC simulations, on which the KH instability grows at a lower rate. Since this study is mostly focused on the nonlinear stage, a smaller initial perturbation is applied to the fluid simulation to make both systems almost simultaneously arrive to the nonlinear stage at about t = 75, which is convenient for a detailed comparison.

The anomalous viscosity for both fluid and hybrid simulation correlates to the growth of KH until the early nonlinear stage (i.e., $t \approx 100$), and both reach their peak value when the instability saturates. In the late nonlinear stage (i.e. t > 150), the anomalous viscosity value becomes scattered, which is likely affected by secondary small-scale processes (e.g., magnetic reconnection) driven by the KH mode. The fluid simulation shows that the magnetic island is switched on at $t \approx 110$, and the total magnetic island area, A_r , remains over 500 after t = 150. The magnetic island fully depends on the tiny diffusion point, requiring a thin current layer, which can be widened by the KH dynamics and consequently switch off reconnection. Therefore, there are several sharp jumps between t = 100 and 150 in

panel C, and this process can be exaggerated by the nonlinear resistivity model. Thus it should not be considered as a robust feature. In contrast, the hybrid simulation gradually increases the magnetic island area and saturates at a smaller value (≈ 100) compared to the fluid result. The mixed area from fluid with test particle simulation and hybrid simulation are identical until t=150. The smaller amplitude oscillation in this interval is due to the ion gyroradius motion. The missing feedback from the test particles to the electromagnetic field in the fluid simulation allows for an additional artificial mixing such that the fluid mixing is larger in the final stages of the simulation.

263

264

266

268

269

270

271

272

273

274

275

277

283

284

285

286

287

288

290

292

293

294

295

296

298

299

Matsumoto and Hoshino [2006] used a similar initial configuration but without magnetic B_y components, in which the mixed region is defined as $A_m = \int r_M dx dy$. This definition of mixed region has only a minor difference compared to our definition. The final diffusion width (i.e., mixed region normalized by the KH wavelength) is almost identical between our hybrid simulation results and their full particle simulation, although we used about twice the KH wavelength. This result suggested that for the given magnetosheath and magnetosphere conditions, the final diffusion layer is insensitive to the KH wavelength.

Figure 2 shows the selected results of fluid with test particle simulation. The top two panels show plasma density, ρ (color index), in-plane velocity, u_x and u_y (white arrows), and magnetic field lines (black lines) at t = 108 (left) and 162 (right). The bottom two panels show the plasma mixing rate, r_M (color index) at t = 108 (left) and 162 (right). The white contour lines highlight $r_M = 0.5$ (i.e., the definition of mixed area $r_M \geq 0.5$), and magenta lines are the boundary of magnetic islands formed by magnetic reconnection. There is a clear vortex structure with a thin spine region in the middle of the simulation box at the early nonlinear stage (e.g., t = 108), while the neighboring vortices begin to collapse to a broad boundary layer at the later nonlinear stage (e.g., t = 162). Although the magnetic field has been strongly bent at t = 108, the current sheet is not sufficiently thin to trigger magnetic reconnection, therefore, no magnetic island is formed at that moment. After the onset of magnetic reconnection, the majority of the vortex region becomes magnetic island. In contrast, the description of particle motion using test particles in the fluid simulation shows the mixing of particles has already operated along the interface between the two sides of fluid at t = 108. Thus, the highly mixed region (i.e., the yellow belt bounded by the white lines) highlights the strongly modified boundary layer. The width of the yellow belt (i.e. mixed area) is close to the gyroradius,

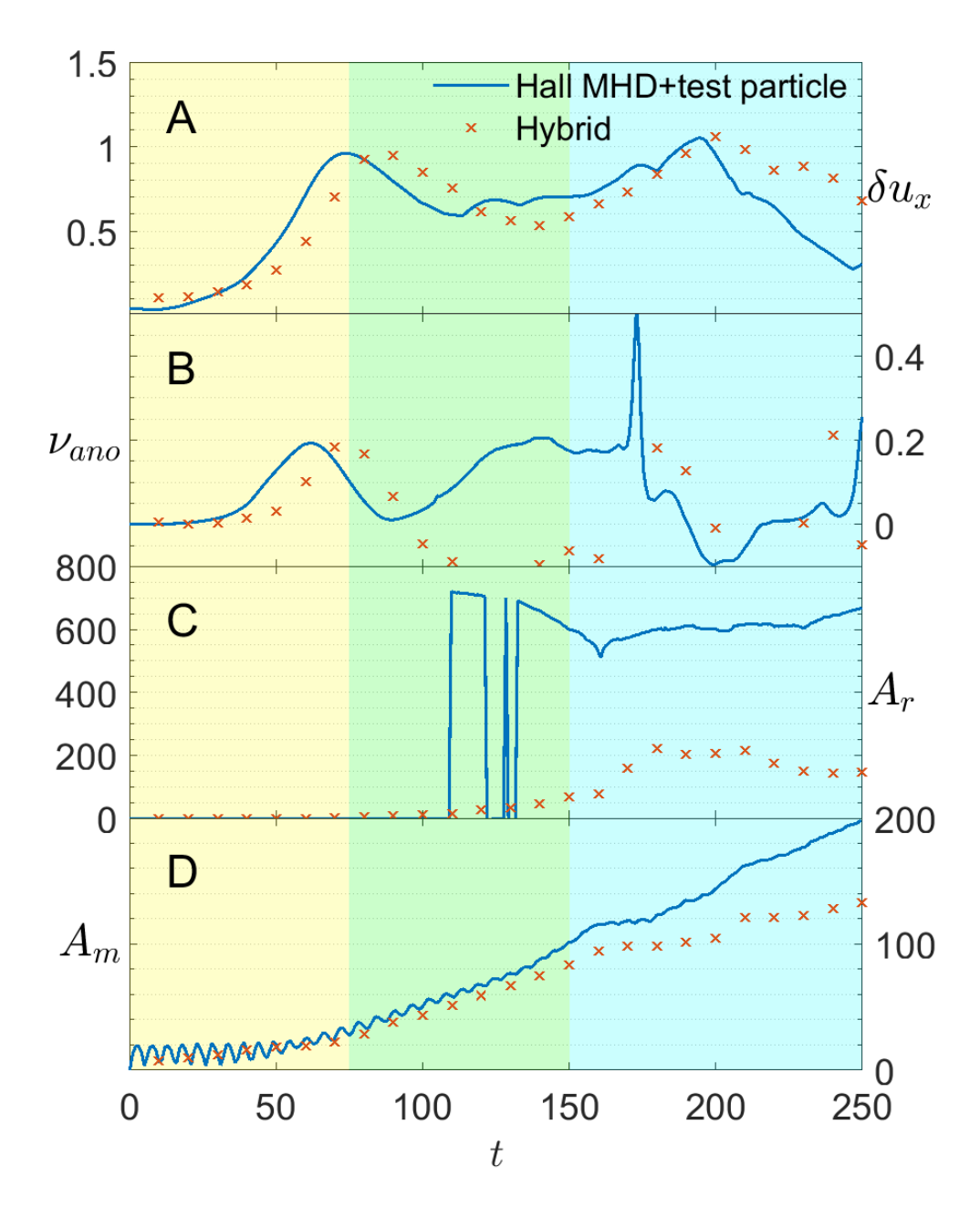


Figure 1. Fluid with test particle (blue lines) and hybrid simulation (red crosses) results of velocity u_X component, the anomalous viscosity, v_{ano} , the area of magnetic island, A_r , and the area of mixed area, A_M , as functions of time from top to bottom, respectively. The yellow, green, and cyan background indicate linear stage ($t \le 75$), early nonlinear stage ($t \le 150$), and later nonlinear stage (t > 150).

280

281

which appears insensitive to the time. Thus, the increase of the mixed area is mainly due to the extension of the length of interface, which is caused by the KH instability. This result agrees with the previous hybrid simulation by *Terasawa et al.* [1992] and *Thomas and Winske* [1993]. Note that the mixed region barely overlaps with the magnetic island, because these two concepts describe two fundamentally different physics processes.

300

301

303

305

307

308

309

310

311

312

314

316

317

318

319

320

331

332

333

335

336

337

338

339

340

341

342

As comparison, Figure 3 mimics Figure 2 showing the selected results from the hybrid simulation at similar times t = 110 (left) and 160 (right). The hybrid simulation results are mostly identical to the fluid and test particle results. However, both the size and the location of magnetic island are different between fluid and hybrid simulations. The fluid simulation forms relatively fewer but larger scale magnetic islands, and their formation fully depends on the few tiny localized reconnection sites. For hybrid simulation, the size of magnetic islands is smaller, and they exist not only inside of the vortex but also along the spine region, suggesting that the magnetic diffusion region becomes very patchy in the hybrid simulation, which is likely due to the kinetic physics missing in the fluid description and numeric noise [Henri et al., 2013]. The difference does not have a strong influence at the early nonlinear stage, since the thin current layers only appear in a small region (e.g., spine or part of the vortex region). Nevertheless, with the continuous twisting of magnetic field lines, KH modes eventually form multiple thin current layers inside of the vortex region, where the missing kinetic physics becomes important and fluid simulations often exaggerate the diffusion region. This is likely the reason why fluid with test particle simulation gives a higher mixed area.

In general, the particle distribution moments from the test particle simulation should represent the fluid results. However, it is more interesting to examine whether the anisotropic particle distribution from the test particle simulation is comparable to the result from hybrid simulation. In test particle and hybrid simulations, the temperature tensor, T_{ij} , can be evaluated by calculating the second moment of the particles' velocity distribution (i.e., the standard deviation of particles' velocity, $T_{ij} = \overline{(v_i^l - \bar{v_i})(v_j^l - \bar{v_j})}$, where the overline represents the average based on all the individual particles within the selected area), which is coordinate dependent. Nevertheless, it is easy to find the highest and lowest temperature and their directions by using the minimum or maximum variance analysis (MVA) [Sonnerup and Scheible, 1998]. For quantification of this property, all particles within a distance of d = 0.2 from the given point (x_0, y_0) are selected to evaluate the anisotropic value, λ_3/λ_1 at the point (x_0, y_0) , where λ_3 and λ_1 are the maximum and minimum eigen-

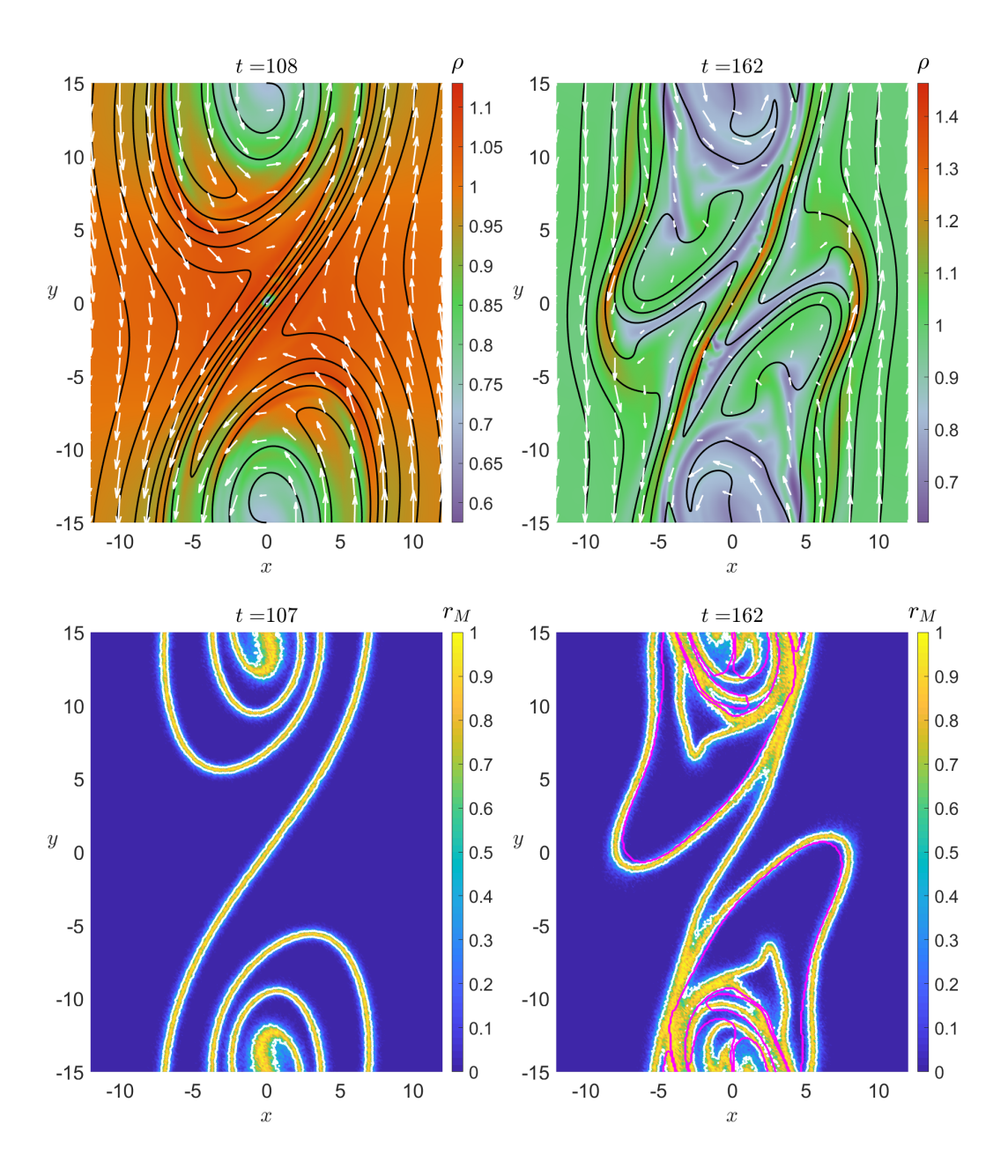


Figure 2. Selected results of fluid with test particle simulation. The top two panels show plasma density, ρ (color index), in-plane velocity, u_x and u_y (white arrows), and magnetic field lines (black lines) at t=108 (left) and 162 (right). The bottom two panels show the plasma mixing rate, r_M (color index) at t=108 (left) and 162 (right). The white contour lines highlight $r_M=0.5$, and magenta lines are the boundary of magnetic islands formed by magnetic reconnection.

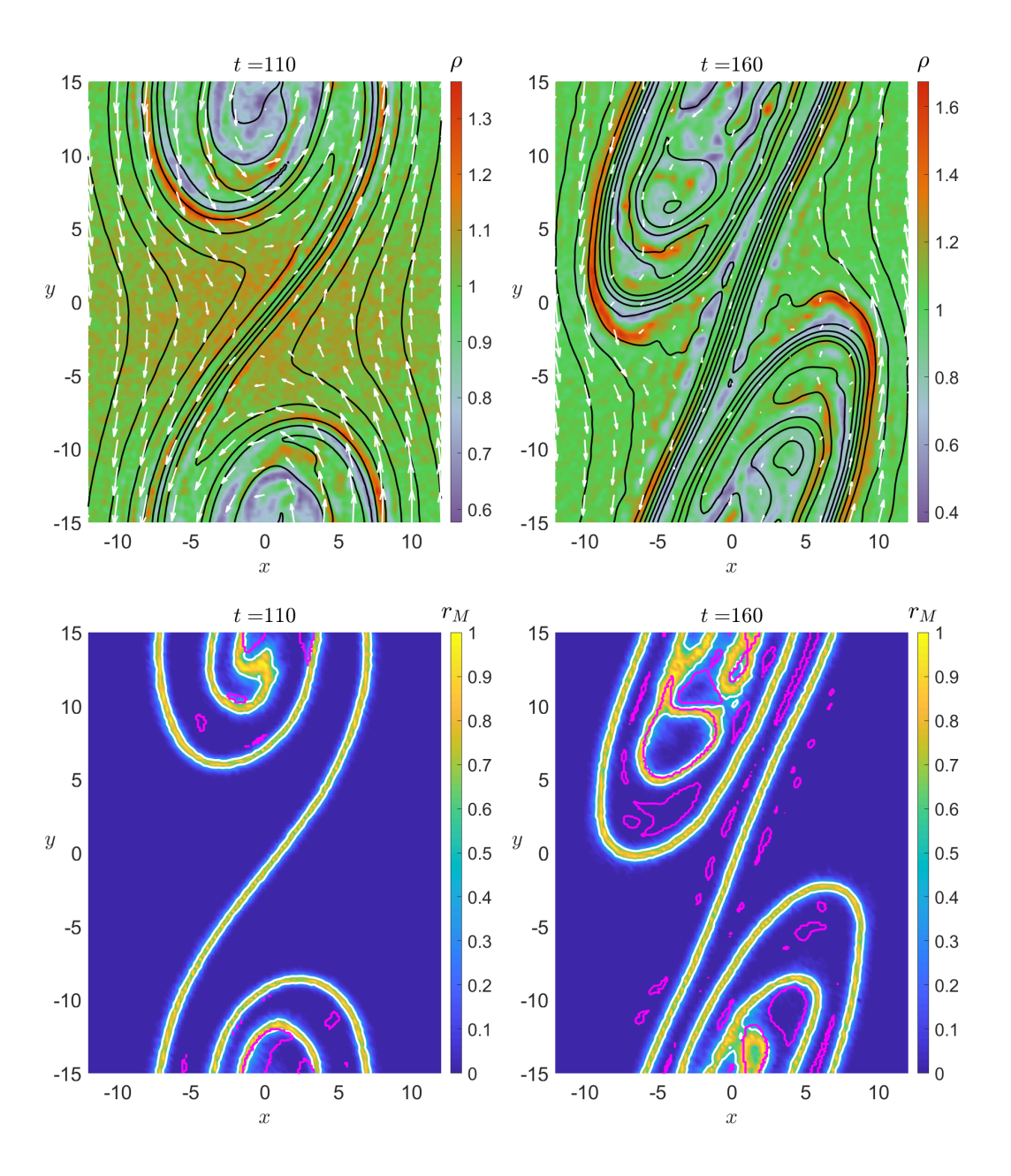


Figure 3. Selected results of hybrid simulation. The top two panels show plasma density, ρ (color index) and in-plane velocity, u_x and u_y (white arrows), and magnetic field lines (black lines) at t=110 (left) and 160 (right). The bottom two panels show the plasma mixing rate, r_M (color index) at t=110 (left) and 160 (right). The white contour lines highlight $r_M=0.5$, and magenta lines are the boundary of magnetic island formed by magnetic reconnection.

327

329

values from the MVA method based on all three velocity components of selected particles. These eigenvalues represent the maximum and minimum standard deviation of the particles' velocities. Therefore, the anisotropic value here means the ratio between highest and lowest temperature for a given point, which does not tell whether the direction of highest or lowest temperature is along the magnetic field or not. Figure 4 shows the anisotropic value, λ_3/λ_1 , for fluid with test particle simulation (left) and hybrid simulation (right) at early nonlinear stage (top) and later nonlinear stage (bottom). The results from test particles quantitatively agree with the hybrid simulations, although the hybrid simulation has a slightly smaller maximum anisotropic value. Both simulations show the anisotropic value increase at shear flow boundary with the growth of the KH instability. The highest value is often in the spine region. It is interesting to note that there is no strong gradient of bulk velocity in the spine region (see Figure 2 and 3), therefore, the high anisotropic value is not due to counter streaming.

As a comparison, Figure 5 plots the ratio between parallel and perpendicular temperature, T_{\parallel}/T_{\perp} . The test particle simulation agrees well with the hybrid simulation at the early nonlinear stage, however, there is large deviation in the vortex region at the later nonlinear stage. For instance, the test particle simulation shows $T_{\parallel} > T_{\perp}$ in the vortex region, while hybrid simulation shows T_{\parallel} lower than T_{\perp} in the same region. Note in Figure 4, these two simulations have similar λ_3/λ_1 value in the vortex region, meaning this deviation may be attributed to the different magnetic field directions in fluid and hybrid simulations. Nevertheless, both simulations show perpendicular temperature is greater than the parallel temperature in the spine region, which is a robust feature. This anisotropic temperature is likely to driven small scale kinetic waves (e.g., mirror modes and ion cyclotron waves [*Nykyri et al.*, 2003, 2011; *Dimmock et al.*, 2015, 2017]) and secondary instabilities (e.g., firehose instability).

The double-adiabatic theory is often used for describing an anisotropic MHD system, which assumes that the specific entropy, $s=\frac{T_\perp^2T_\parallel}{\rho^2}$, and the magnetic moment, $\mu=\frac{mv_\perp^2}{2B}$, are conserved along the trajectory of a fluid parcel. Here, v_\perp is the particle's perpendicular velocity. Thus, the equation of state can be rewritten as ds/dt=0, and dh/dt=0, where the parallel term is $h=\frac{T_\parallel B^2}{\rho^2}$, and the material derivative, d/dt, is based on bulk velocity. Figure 6 shows the change of specific entropy, s/s_0 (top), and the parallel term h/h_0 (bottom), in logarithmic scale at t=120 (left) and 160 (right) from hybrid stimulation, suggesting that neither specific entropy nor the parallel term is conserved. Here,

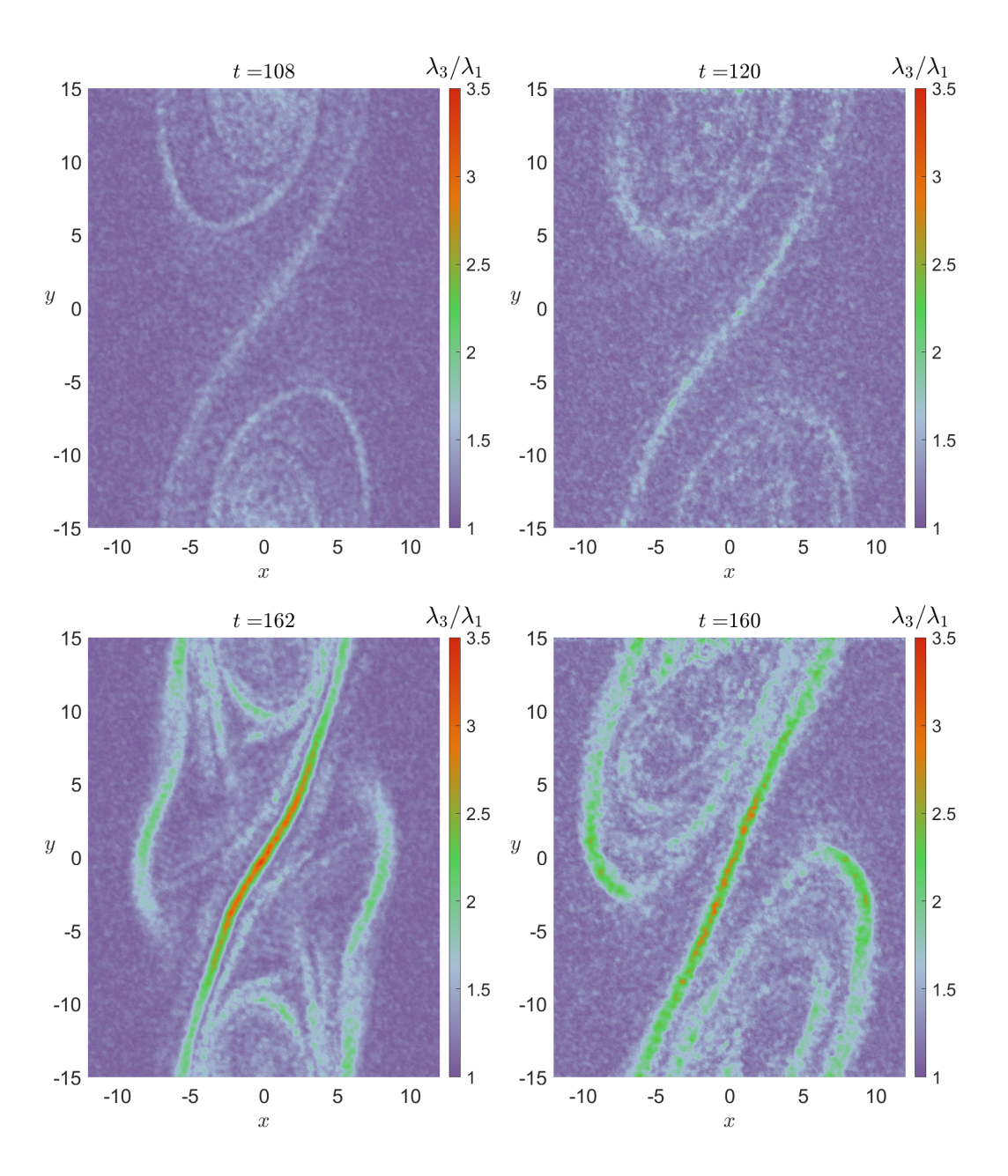


Figure 4. The anisotropic value, λ_3/λ_1 , for fluid with test particle simulation (left) and hybrid simulation (right) at early nonlinear stage (top) and later nonlinear stage (bottom).

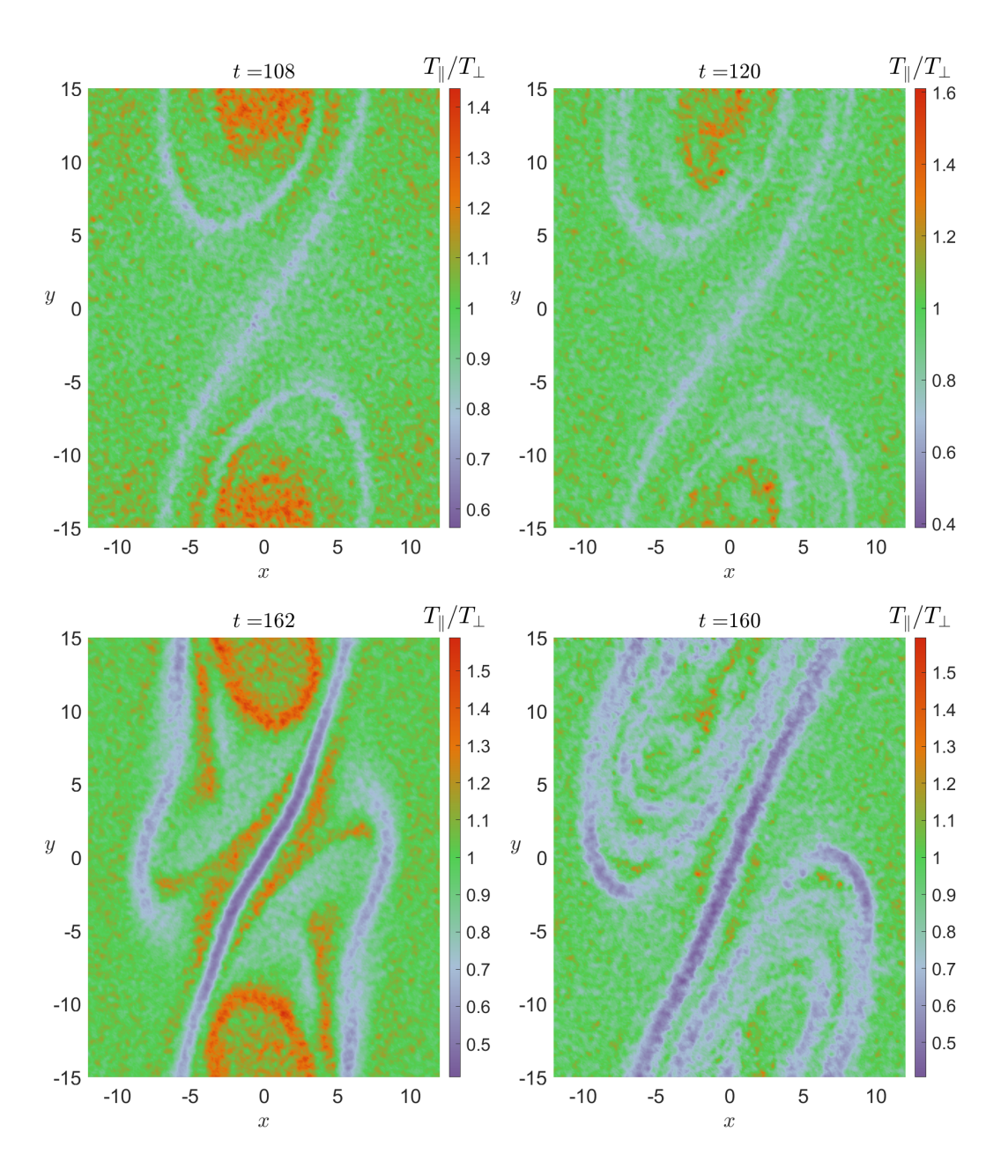


Figure 5. The ratio of parallel and perpendicular temperature, T_{\parallel}/T_{\perp} , for fluid with test particle simulation (left) and hybrid simulation (right) at early nonlinear stage (top) and later nonlinear stage (bottom).

the subscript 0 refers to the initial values. The test particle simulation results are not presented here, because it is mostly identical to the hybrid result. The specific entropy increases by half an order of the magnitude at the early nonlinear stage to one order of the magnitude at the later nonlinear stage along the spine region and in the KH vortex region. This implies nonadiabatic heating processes are triggered in the KH instability, which includes but is not limited to magnetic reconnection. Nevertheless, the specific entropy enhancement is still less than the observation [*Ma and Otto*, 2014]. The parallel term has relatively smaller enhancement, and it can also decrease in the edge of the vortex region, suggesting the first adiabatic invariant is no longer conserved in this condition.

380

381

383

385

387

388

391

393

394

399

401

403

405

406

407

408

409

410

The top panels of Figure 7 show the average change of magnetic moment, $\log(\frac{\overline{\mu}}{\mu_0})$, where the subscript 0 refers to the initial values, and over-line refers to the geometric mean for all particles near the given point within a distance d = 0.2. The change of magnetic moment can be roughly expressed as follows (see detailed derivation in appendix):

$$\frac{d}{dt} \left(\frac{v_{\perp}^2}{B} \right) = \frac{2}{B} \gamma \mathbf{v}_{\perp} \cdot \mathbf{E}_{\perp} + \left(\frac{2v_{\parallel} \mathbf{v}_{\perp} + v_{\perp}^2 \mathbf{b}}{B^2} \right) \cdot (\nabla \times \mathbf{E} - \mathbf{v} \cdot \nabla \mathbf{B}), \tag{1}$$

where $\gamma = q/m$ is the charge-to-mass ratio. This can be interpreted as the contribution of the perpendicular electric field, the magnetic field temporal variation (i.e, curl of the electric field), and the magnetic field spatial variations along the particle trajectory. Presuming that the guiding center of ions are roughly moving at bulk velocity, the test particle simulation suggests that ion magnetic moments first decrease when ions are approaching the spine region. Then, their magnetic moments increase along the spine region and eventually drift into the KH vortex region. It is also interesting to note that the magnetic moment increase region coincides with the mixing region. In contrast, the bottom panels of Figure 7 show the average change of ion kinetic energy in the drift frame, E_d (i.e., the square of ion velocity subtracting the $\mathbf{E} \times \mathbf{B}$ drift velocity), indicating plasma heating, which mainly increases in the spine region and decreases in the KH vortex region. The maximum increase of kinetic energy is about a half order of magnitude (i.e., $10^{0.5} \approx 3$). As a comparison, the typical magnetosheath ion temperature is about 100 eV on the dawn and dusk flank terminator [Dimmock et al., 2015], while the ion temperature in the cold and dense plasma sheet (CDPS) is close to 1 keV (see [Wing et al., 2014] and references therein).

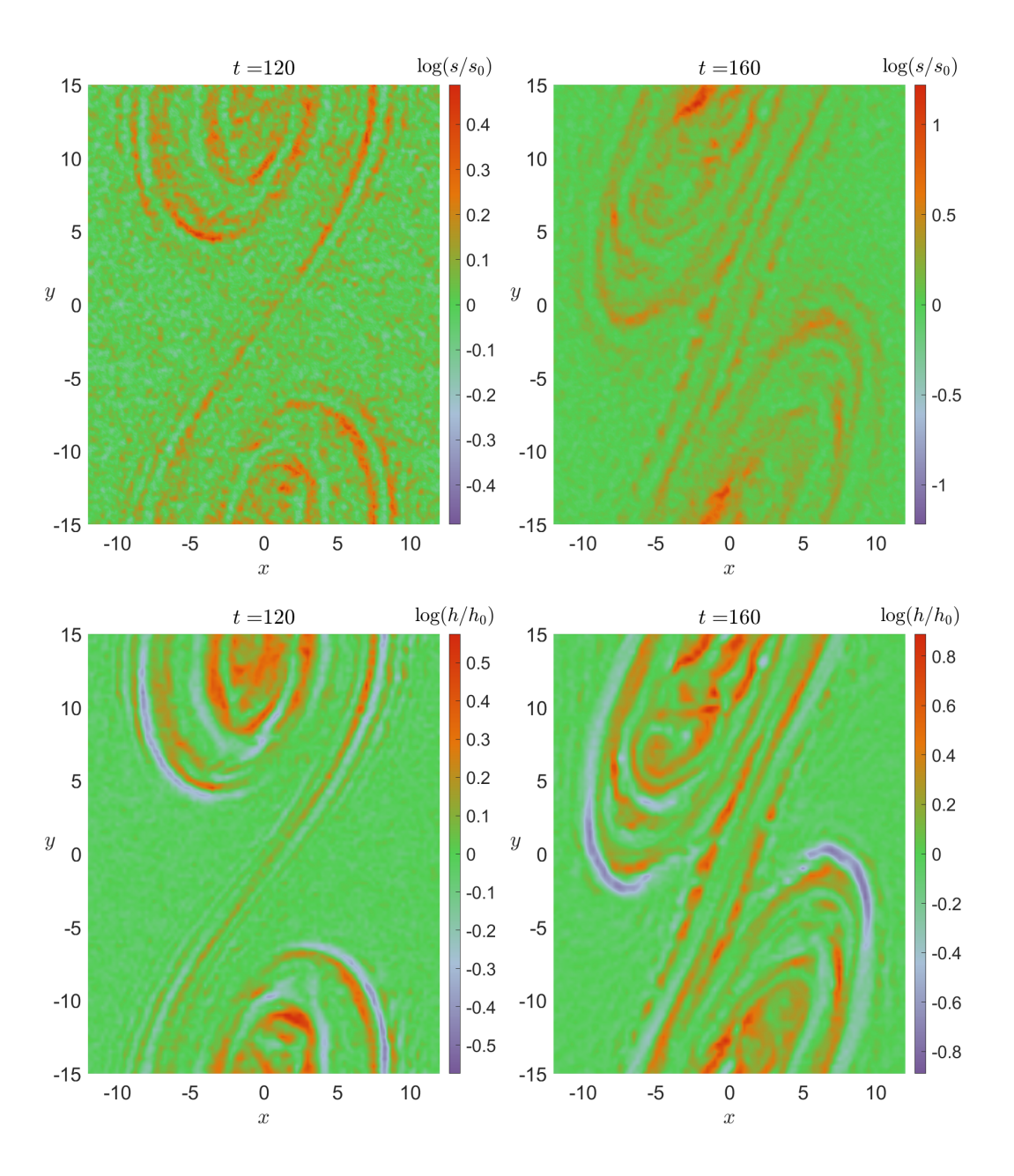


Figure 6. The change of the specific entropy (top) and the parallel term (bottom) in logarithmic scale at t = 120 (left) and 160 (right) from hybrid stimulation.

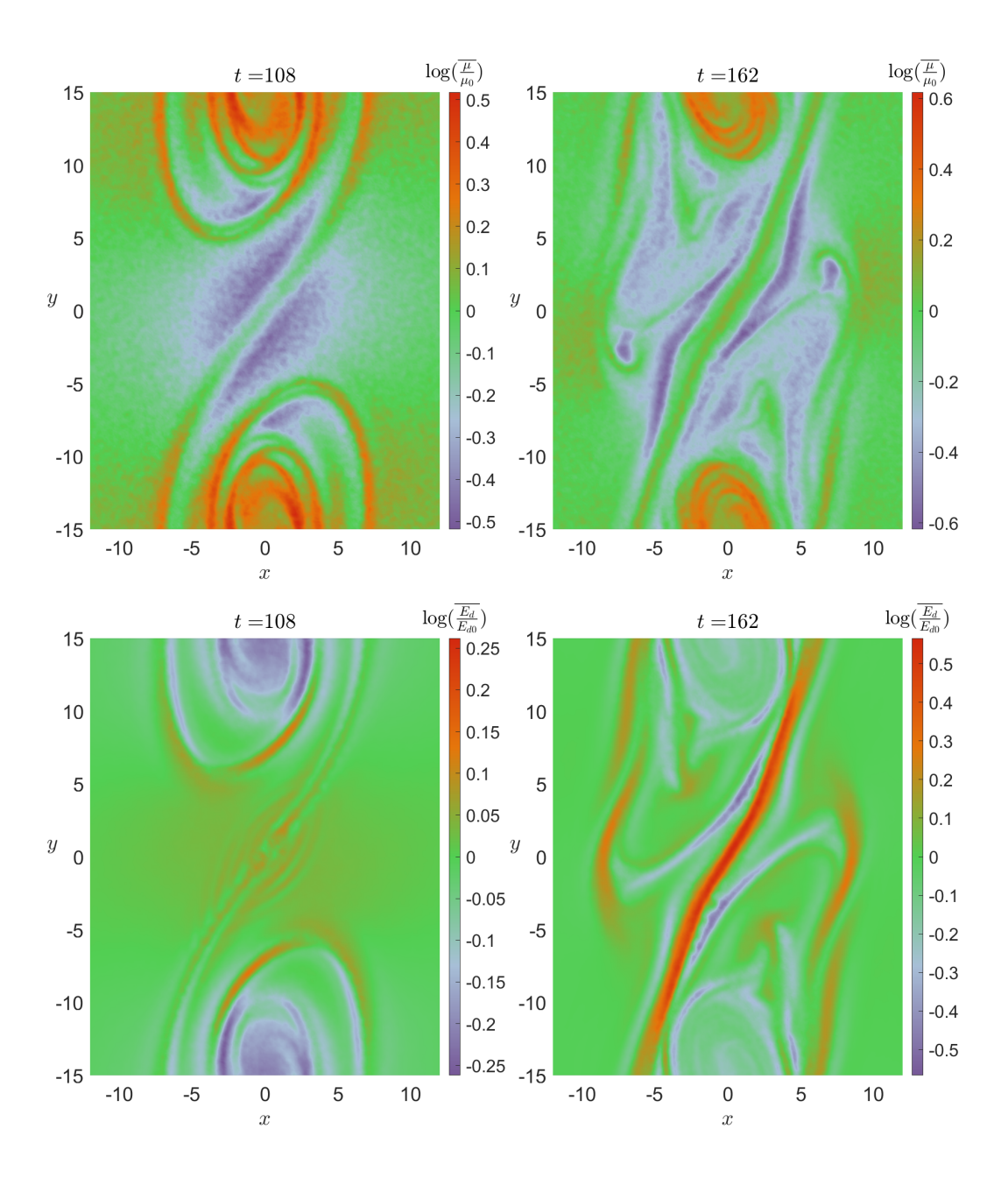


Figure 7. The geometric mean of magnetic moment enhancement (top) and kinetic energy enhancement in the $\mathbf{E} \times \mathbf{B}$ drift frame (bottom) at early nonlinear stage (left) and later nonlinear stage (right).

4 Summary and Discussion

This study carefully compared the results from Hall MHD with test particle and hybrid simulations for the KH instability. Instead of investigating the path of each individual ion with a certain energy range, we focused on the macro-scale properties of the ions, namely, the mixing rate, temperature anisotropy, the average magnetic moment, and the average kinetic energy in the $\mathbf{E} \times \mathbf{B}$ drift frame.

- 1. In the current test parameter regime, Hall MHD with test particles and hybrid simulation give almost identical particle mixing rates. The increase of particle mixing is largely determined by the extension of the sheared flow interface length of the KH instability. The overall mixed area is smaller than the reconnected magnetic island area in Hall MHD, but much greater than the magnetic island area in hybrid simulations, suggesting that particle mixing by finite gyro-radius is the dominant process in the hybrid simulations. However, it is important to keep in mind that the measurement of particle mixing in the 2-D geometry and the 3-D geometry with periodic boundary conditions along the third dimension should not be interpreted as the measurement of the amount of plasma transport from the MSH into the MSP, because one cannot identify whether these mixing regions are eventually connected to the MSH or the MSP. Thus, a careful quantification of plasma transport must define a boundary between the MSH and the MSP based on the magnetic field configuration first, and then compare the mass change within these regions (e.g. *Ma et al.* [2017]; *Sorathia et al.* [2017]).
- 2. The nonlinear KH instability can cause anisotropic temperature. Two different types of temperature anisotropy values are used in this study, that is the ratio of the maximum and minimum eigenvalues of matrix by using the MVA method based on three components of selected particles' velocities, λ_3/λ_1 , and the ratio of the parallel and the perpendicular temperature, T_{\parallel}/T_{\perp} . Note that $\lambda_3/\lambda_1 \geqslant \max{(T_{\parallel}/T_{\perp}, T_{\perp}/T_{\parallel})}$. Both test particle and hybrid simulations show almost identical results for λ_3/λ_1 and T_{\parallel}/T_{\perp} during the early nonlinear stage and even in the spine region during the later nonlinear stage, implying that $T_{\parallel}/T_{\perp} < 1$ in the spine region is a robust feature. A large deviation appears for T_{\parallel}/T_{\perp} in the vortex region in the later nonlinear stage. Notice, the measurement of λ_3/λ_1 is independent from the measurement of the magnetic field. Therefore, the deviation of T_{\parallel}/T_{\perp} between test particles and hybrid simulation is likely to be caused by the different magnetic field configuration obtained from these two types of simulation. Nevertheless, the

nonlinear KH instability significantly increases the anisotropic value, λ_3/λ_1 , in the spine and vortex regions, which can potentially be used to identify whether the in-situ observed KH event is in the early nonlinear stage or later nonlinear stage. The highly anisotropic temperature regions formed within KH waves are expected to give rise to the firehose, mirror or ion-cyclotron modes. However, the present results are somewhat limited by the 2-D geometry in this study, because, the magnetic field is mostly along the invariable direction (i.e., $k_{\parallel}=0$). Thus, for realistic observation, the maximum and minimum ratio of parallel and perpendicular temperature is likely to be limited by the firehose mode or mirror mode onset condition.

- 3. Compared with double-adiabatic theory, neither specific entropy nor the parallel term is conserved in the nonlinear KH wave, suggesting both adiabatic and nonadiabatic heating/cooling processes happen along the parallel direction. Thus, a more sophisticated equation of state (e.g., [Meng et al., 2012; Wang et al., 2015]) is desired to resolve meso-scale process (e.g., KH instability) for a better understanding of the multi-scale coupling process. The anisotropic velocity distribution is often associated with particle gyro-motion, in which the first adiabatic invariant, the magnetic moment, is the important quantity to be investigated. It is expected that the magnetic moment is no longer conserved, because the presence of the electric field, and the temporal and spatial variation of the magnetic field along the particle trajectory. The test particle simulation suggests that the magnetic moment often decreases before particles drifts into the spine region and increases along the spine region into the vortex region.
- 4. The average magnetic moment pattern appears in contrast with the drift frame kinetic energy, E_d , which increases in the spine region and decreases in the vortex region. The drift frame kinetic energy, E_d , is representative of particle heating, implying ions can be heated in the spine region, but by only half an order of magnitude at most, which is very different from the observation.

Based on this numerical experiment, the test particle simulation appears to provide an accurate description of particle properties (e.g., diffusion rate and anisotropy temperature) during the KH instability, especially at the early nonlinear stage. Although, at the later nonlinear stage, small structure formed by the KH vortex eventually requires a hybrid simulation or even a fully PIC simulation. Practically, for in-situ observations, the early nonlinear stage of KH vortex often has a relatively clear observational signature to iden-

tify. Thus, the fluid simulation with test particle is a good method to compare with the observation.

Nevertheless there are several important observational features which have not been included in our simulation configuration. For instance, at the Earth's magnetopause, the magnetic field and density are highly asymmetric. It is not clear whether the nonadiabatic heating process in the KH instability favors low temperature/plasma beta particles. Furthermore, the KH instability in three dimensions is fundamentally different from the two-dimensional geometry. It has been suggested that the middle-latitude double reconnection process can provide an additional nonadiabatic heating source [Johnson and Wing, 2009], which will be investigated in our future study.

A: Derivation of Equation 1

477

478

480

481

482

484

485

486

487

489

490

From the definition of magnetic moment, we have

$$\frac{d}{dt} \left(\frac{v_{\perp}^2}{B} \right) = \frac{1}{B} \frac{d}{dt} \left(v_{\perp}^2 \right) - \frac{v_{\perp}^2}{B^2} \frac{dB}{dt} \tag{A.1}$$

$$= \frac{1}{B} \frac{d}{dt} \left(v^2 - v_{\parallel}^2 \right) - \frac{v_{\perp}^2}{B^2} \frac{dB}{dt}, \tag{A.2}$$

where, $d/dt = \partial/\partial t + \mathbf{v} \cdot \nabla$ represents the variation along the particle trajectory. The derivative of total energy v^2 with respective to time can be found from

$$\frac{dv^2}{dt} = 2\mathbf{v} \cdot \frac{d\mathbf{v}}{dt} \tag{A.3}$$

$$=2\mathbf{v}\cdot\gamma\left(\mathbf{v}\times\mathbf{B}+\mathbf{E}\right)\tag{A.4}$$

$$=2\gamma\mathbf{v}\cdot\mathbf{E}.\tag{A.5}$$

The equation of parallel velocity is

$$\frac{dv_{\parallel}}{dt} = \frac{d}{dt} \left(\mathbf{v} \cdot \mathbf{b} \right) \tag{A.6}$$

$$= \frac{d\mathbf{v}}{dt} \cdot \mathbf{b} + \mathbf{v} \cdot \frac{d\mathbf{b}}{dt} \tag{A.7}$$

$$= \gamma \left(\mathbf{v} \times \mathbf{B} + \mathbf{E} \right) \cdot \mathbf{b} + \mathbf{v} \cdot \left(\frac{\partial \mathbf{b}}{\partial t} + \mathbf{v} \cdot \nabla \mathbf{b} \right)$$
 (A.8)

$$= \gamma E_{\parallel} + \mathbf{v} \cdot \left(\frac{\partial \mathbf{b}}{\partial t} + \mathbf{v} \cdot \nabla \mathbf{b} \right), \tag{A.9}$$

where **b** is the unit vector of magnetic field **B**. The last term implies that the change of parallel velocity can be due to the change of the magnetic field direction along the particle

- trajectory, even without temporal variation of the magnetic field (i.e., adiabatic motion
- assumption). Thus, the last term is expected to be close to the mirror force, $-\frac{v_{\perp}^2}{2B}\mathbf{b} \cdot \nabla B$,
- when the gyroradius is much smaller than the $|B/(\nabla B)|$. Notice that:

$$\nabla \cdot B = \mathbf{b} \cdot \nabla B + B \nabla \cdot \mathbf{b} = 0$$
.

such that the mirror force can also be rewritten as $\frac{v_1^2}{2}\nabla \cdot \mathbf{b}$.

With the help of Equation A.5 and A.9, Equation A.2 can be rewritten as:

$$\frac{d}{dt} \left(\frac{v_{\perp}^2}{B} \right) = 2\frac{1}{B} \left(\gamma \mathbf{v} \cdot \mathbf{E} - \gamma v_{\parallel} E_{\parallel} - v_{\parallel} \mathbf{v} \cdot \frac{d\mathbf{b}}{dt} \right) - \frac{v_{\perp}^2}{B^2} \frac{dB}{dt}$$
(A.10)

$$= \frac{2}{B} \gamma \mathbf{v}_{\perp} \cdot \mathbf{E}_{\perp} - \left(\frac{2\nu_{\parallel} \mathbf{v}_{\perp} + \nu_{\perp}^{2} \mathbf{b}}{B^{2}} \right) \cdot \left(\frac{\partial \mathbf{B}}{\partial t} + \mathbf{v} \cdot \nabla \mathbf{B} \right)$$
(A.11)

$$= \frac{2}{B} \gamma \mathbf{v}_{\perp} \cdot \mathbf{E}_{\perp} + \left(\frac{2\nu_{\parallel} \mathbf{v}_{\perp} + \nu_{\perp}^{2} \mathbf{b}}{B^{2}} \right) \cdot (\nabla \times \mathbf{E} - \mathbf{v} \cdot \nabla \mathbf{B}). \tag{A.12}$$

- Comparing with $d\mu/dt = 0$ for adiabatic motion $(\mathbf{v}_{\perp} \cdot \mathbf{E}_{\perp} = 0)$ in the sense of one periodic
- gyro-motion, and $\partial/\partial_t = 0$), the term associated $d/dt \approx \mathbf{v} \cdot \nabla$ should be negligible under
- the adiabatic motion assumption.

Acknowledgments

498

506

- The work of X. M. and P. D. is supported from NASA grants 80NSSC18K1108.
- Work by K. N. is supported by NASA grant NX17A150G. The work of B. B. and B.N. is
- supported by NASA Grant NNX15AH09G. The work of R. R. is supported by NSF Grant
- 502 1707521. The model source code in this paper can be accessed at https://github.com/padelamere.
- The simulation data and visualization tools in this paper can be accessed from https://commons.erau.edu/.
- We are grateful to the International Space Science Institute (ISSI) for their support to the
- Coordinated Numerical Modeling of the Global Jovian and Saturnian Systems team.

References

- Arfken, G. (1985), Mathematical Methods for Physicists, third ed., Academic Press, Inc.,
- 508 San Diego.
- Birdsall, C. K., and A. B. Langdon (1991), Plasma Physics via Computer Simulation.
- Birn, J. (1980), Computer studies of the dynamic evolution of the geomagnetic tail, *Jour-*
- nal of Geophysical Research, 85, 1214–1222, doi:10.1029/JA085iA03p01214.
- Birn, J., M. F. Thomsen, J. E. Borovsky, G. D. Reeves, D. J. McComas, R. D. Belian, and
- M. Hesse (1997), Substorm ion injections: Geosynchronous observations and test par-

- ticle orbits in three-dimensional dynamic mhd fields, Journal of Geophysical Research:
- 515 Space Physics, 102(A2), 2325–2341, doi:10.1029/96JA03032.
- Birn, J., M. F. Thomsen, J. E. Borovsky, G. D. Reeves, D. J. McComas, R. D. Belian, and
- M. Hesse (1998), Substorm electron injections: Geosynchronous observations and test
- particle simulations, Journal of Geophysical Research: Space Physics, 103(A5), 9235–
- 9248, doi:10.1029/97JA02635.
- Borgogno, D., F. Califano, M. Faganello, and F. Pegoraro (2015), Double-reconnected
- magnetic structures driven by Kelvin-Helmholtz vortices at the Earth's magnetosphere,
- *Physics of Plasmas*, 22(3), 032301, doi:10.1063/1.4913578.
- Boris, J. (1970), The Acceleration Calculation From a Scalar Potential, Princeton Univer-
- sity Plasma Physics Laboratory.
- ⁵²⁵ Cowee, M. M., D. Winske, and S. P. Gary (2009), Two-dimensional hybrid simulations of
- superdiffusion at the magnetopause driven by Kelvin-Helmholtz instability, Journal of
- Geophysical Research (Space Physics), 114, A10209, doi:10.1029/2009JA014222.
- ⁵²⁸ Cowee, M. M., D. Winske, and S. P. Gary (2010), Hybrid simulations of plasma trans-
- port by Kelvin-Helmholtz instability at the magnetopause: Density variations and
- magnetic shear, Journal of Geophysical Research (Space Physics), 115, A06214, doi:
- 10.1029/2009JA015011.
- Delamere, P. A. (2009), Hybrid code simulations of the solar wind interaction with
- pluto, Journal of Geophysical Research: Space Physics, 114(A3), n/a-n/a, doi:
- 10.1029/2008JA013756, a03220.
- Delamere, P. A., D. W. Swift, and H. C. Stenbaek-Nielsen (1999), A three-dimensional
- hybrid code simulation of the december 1984 solar wind ampte release, Geophysical
- Research Letters, 26(18), 2837–2840, doi:10.1029/1999GL900602.
- Delamere, P. A., R. J. Wilson, and A. Masters (2011), Kelvin-helmholtz instability at
- saturn's magnetopause: Hybrid simulations, Journal of Geophysical Research: Space
- Physics, 116(A10), n/a-n/a, doi:10.1029/2011JA016724, a10222.
- Delamere, P. A., B. B., and M. X. (2018), Three-dimensional hybrid simulation of
- viscous-like processes at saturn's magnetopause boundary, Geophysical Research Let-
- 543 ters, 45(ja).
- Dimmock, A. P., K. Nykyri, H. Karimabadi, A. Osmane, and T. I. Pulkkinen (2015), A
- statistical study into the spatial distribution and dawn-dusk asymmetry of dayside mag-
- netosheath ion temperatures as a function of upstream solar wind conditions, Journal of

- Geophysical Research: Space Physics, 120(4), 2767–2782, doi:10.1002/2014JA020734.
- Dimmock, A. P., A. Osmane, T. I. Pulkkinen, K. Nykyri, and E. Kilpua (2017), Temper-
- ature variations in the dayside magnetosheath and their dependence on ion-scale mag-
- netic structures: Themis statistics and measurements by mms, Journal of Geophysical
- Research: Space Physics, 122(6), 6165–6184, doi:10.1002/2016JA023729.
- Faganello, M., F. Califano, and F. Pegoraro (2009), Being on time in magnetic reconnec-
- tion, New Journal of Physics, 11(6), 063,008, doi:10.1088/1367-2630/11/6/063008.
- Faganello, M., F. Califano, F. Pegoraro, and T. Andreussi (2012), Double mid-latitude
- dynamical reconnection at the magnetopause: An efficient mechanism allowing solar
- wind to enter the earth's magnetosphere, EPL (Europhysics Letters), 100(6), 69,001, doi:
- 10.1209/0295-5075/100/69001.
- Harned, D. S. (1982), Quasineutral hybrid simulation of macroscopic plasma phenomena,
- Journal of Computational Physics, 47, 452–462, doi:10.1016/0021-9991(82)90094-8.
- Henri, P., S. S. Cerri, F. Califano, F. Pegoraro, C. Rossi, M. Faganello, O. Šebek, P. M.
- Trávníček, P. Hellinger, J. T. Frederiksen, A. Nordlund, S. Markidis, R. Keppens,
- and G. Lapenta (2013), Nonlinear evolution of the magnetized kelvin-helmholtz in-
- stability: From fluid to kinetic modeling, *Physics of Plasmas*, 20(10), 102,118, doi:
- 10.1063/1.4826214.
- Henry, Z. W., N. K., M. T. W., D. A. P., and M. X. (2017), On the dawn-dusk asymme-
- try of the kelvin-helmholtz instability between 2007 and 2013, Journal of Geophysical
- search: Space Physics, 122(12), 11,888–11,900, doi:10.1002/2017JA024548.
- Johnson, J., S. Wing, and P. Delamere (2014), Kelvin helmholtz instability in planetary
- magnetospheres, Space Science Reviews, 184(1-4), 1–31, doi:10.1007/s11214-014-0085-
- 570 **Z.**
- Johnson, J. R., and S. Wing (2009), Northward interplanetary magnetic field plasma
- sheet entropies, Journal of Geophysical Research (Space Physics), 114, A00D08, doi:
- 10.1029/2008JA014017.
- Kavosi, S., and J. Raeder (2015), Ubiquity of Kelvin-Helmholtz waves at Earth's magne-
- topause, *Nature Communications*, 6, 7019, doi:10.1038/ncomms8019.
- Ma, X., and A. Otto (2014), Nonadiabatic heating in magnetic reconnection, *Journal of*
- *Geophysical Research (Space Physics)*, 119, 5575–5588, doi:10.1002/2014JA019856.
- Ma, X., A. Otto, and P. A. Delamere (2014a), Interaction of magnetic reconnection and
- Kelvin-Helmholtz modes for large magnetic shear: 1. Kelvin-Helmholtz trigger, *Journal*

- of Geophysical Research: Space Physics, 119(2), 781–797, doi:10.1002/2013JA019224.
- Ma, X., A. Otto, and P. A. Delamere (2014b), Interaction of magnetic reconnection and
- Kelvin-Helmholtz modes for large magnetic shear: 2. reconnection trigger, Journal of
- Geophysical Research: Space Physics, 119(2), 808–820, doi:10.1002/2013JA019225.
- Ma, X., D. Peter, O. Antonius, and B. Brandon (2017), Plasma transport driven by the
- three-dimensional Kelvin-Helmholtz instability, Journal of Geophysical Research: Space
- Physics, 122(10), 10,382–10,395, doi:10.1002/2017JA024394.
- Masson, A., and K. Nykyri (2018), Kelvin–helmholtz instability: Lessons learned and
- ways forward, Space Science Reviews, 214(4), 71, doi:10.1007/s11214-018-0505-6.
- Matsumoto, Y., and M. Hoshino (2006), Turbulent mixing and transport of collisionless
- plasmas across a stratified velocity shear layer, Journal of Geophysical Research: Space
- Physics, 111(A5), doi:10.1029/2004JA010988.
- Meng, X., G. Tóth, M. W. Liemohn, T. I. Gombosi, and A. Runov (2012), Pressure
- anisotropy in global magnetospheric simulations: A magnetohydrodynamics model,
- Journal of Geophysical Research: Space Physics, 117(A8), doi:10.1029/2012JA017791.
- Miura, A. (1984), Anomalous transport by magnetohydrodynamic Kelvin-Helmholtz insta-
- bilities in the solar wind-magnetosphere interaction, Journal of Geophysical Research,
- 89, 801–818, doi:10.1029/JA089iA02p00801.
- Miura, A. (1997), Compressible magnetohydrodynamic kelvin-helmholtz instability with
- vortex pairing in the two-dimensional transverse configuration, *Physics of Plasmas*, 4(8),
- 2871–2885, doi:10.1063/1.872419.
- Miura, A., and P. L. Pritchett (1982), Nonlocal stability analysis of the MHD Kelvin-
- Helmholtz instability in a compressible plasma, Journal of Geophysical Research, 87,
- 7431–7444, doi:10.1029/JA087iA09p07431.
- Moore, T. W., K. Nykyri, and A. P. Dimmock (2016), Cross-scale energy transport in
- space plasmas, *Nature Physics*.
- Nakamura, T. K. M., and W. Daughton (2014), Turbulent plasma transport across the
- earth's low-latitude boundary layer, Geophysical Research Letters, 41(24), 8704–8712,
- doi:10.1002/2014GL061952.
- Nakamura, T. K. M., M. Fujimoto, and A. Otto (2006), Magnetic reconnection induced by
- weak Kelvin-Helmholtz instability and the formation of the low-latitude boundary layer,
- *Geophysical Research Letters*, *33*, 14,106–+, doi:10.1029/2006GL026318.

- Nakamura, T. K. M., H. Hasegawa, and I. Shinohara (2010), Kinetic effects on the Kelvin-
- Helmholtz instability in ion-to-magnetohydrodynamic scale transverse velocity shear
- layers: Particle simulations, *Physics of Plasmas*, 17(4), 042,119, doi:10.1063/1.3385445.
- Nakamura, T. K. M., W. Daughton, H. Karimabadi, and S. Eriksson (2013), Three-
- dimensional dynamics of vortex-induced reconnection and comparison with themis ob-
- servations, Journal of Geophysical Research: Space Physics, 118(9), 5742–5757, doi:
- 618 10.1002/jgra.50547.
- Nakamura, T. K. M., H. Hasegawa, W. Daughton, S. Eriksson, W. Y. Li, and R. Nakamura
- 620 (2017), Turbulent mass transfer caused by vortex induced reconnection in collisionless
- magnetospheric plasmas, Nature Communications, 8(1), 1582, doi:10.1038/s41467-017-
- 622 01579-0.
- Nykyri, K., and A. Otto (2001), Plasma transport at the magnetospheric boundary due
- to reconnection in Kelvin-Helmholtz vortices, Geophysical Research Letters, 28, 3565–
- 3568, doi:10.1029/2001GL013239.
- Nykyri, K., and A. Otto (2004), Influence of the Hall term on KH instability and recon-
- nection inside KH vortices, Annales Geophysicae, 22, 935–949, doi:10.5194/angeo-22-
- 935-2004.
- Nykyri, K., P. J. Cargill, E. A. Lucek, T. S. Horbury, A. Balogh, B. Lavraud, I. Dan-
- douras, and H. Rème (2003), Ion cyclotron waves in the high altitude cusp: Cluster
- observations at varying spacecraft separations, Geophysical Research Letters, 30(24),
- doi:10.1029/2003GL018594.
- Nykyri, K., A. Otto, B. Lavraud, C. Mouikis, L. M. Kistler, A. Balogh, and H. Rème
- 694 (2006), Cluster observations of reconnection due to the Kelvin-Helmholtz instabil-
- ity at the dawnside magnetospheric flank, Annales Geophysicae, 24, 2619–2643, doi:
- 10.5194/angeo-24-2619-2006.
- Nykyri, K., A. Otto, E. Adamson, and A. Tjulin (2011), On the origin of fluctuations in
- the cusp diamagnetic cavity, Journal of Geophysical Research: Space Physics, 116(A6),
- doi:10.1029/2010JA015888.
- Nykyri, K., A. Otto, E. Adamson, E. Kronberg, and P. Daly (2012), On the origin of
- high-energy particles in the cusp diamagnetic cavity, Journal of Atmospheric and Solar-
- 642 Terrestrial Physics, 87, 70–81, doi:10.1016/j.jastp.2011.08.012.
- Nykyri, K., X. Ma, A. Dimmock, C. Foullon, A. Otto, and A. Osmane (2017), Influ-
- ence of velocity fluctuations on the kelvin-helmholtz instability and its associated mass

- transport, Journal of Geophysical Research: Space Physics, 122(9), 9489–9512, doi:
- 10.1002/2017JA024374.
- Ohsawa, Y., K. Nosaki, and A. Hasegawa (1976), Kinetic theory of magnetohydro-
- dynamic kelvin-helmholtz instability, *The Physics of Fluids*, 19(8), 1139–1143, doi:
- 10.1063/1.861620.
- Otto, A. (2001), Geospace Environment Modeling (GEM) magnetic reconnection chal-
- lenge: MHD and Hall MHD-constant and current dependent resistivity models, Journal
- of Geophysical Research, 106, 3751–3758, doi:10.1029/1999JA001005.
- Otto, A. (2006), Mass transport at the magnetospheric flanks associated with three-
- dimensional kelvin-helmholtz modes, in *Eos Trans. AGU*, vol. 87(52), Fall Meet. Suppl.,
- 655 Abstract SM33B-0365.
- Otto, A., and D. H. Fairfield (2000), Kelvin-Helmholtz instability at the magnetotail
- boundary: MHD simulation and comparison with Geotail observations, Journal of Geo-
- physical Research, 105, 21,175–21,190, doi:10.1029/1999JA000312.
- Potter, D. (1973), Computational physics, Wiley-Interscience publication, J. Wiley.
- Pu, Z.-Y., and M. G. Kivelson (1983), Kelvin-helmholtz instability at the magnetopause:
- Energy flux into the magnetosphere, Journal of Geophysical Research: Space Physics,
- 88(A2), 853–861, doi:10.1029/JA088iA02p00853.
- Sonnerup, B. U. Ö., and M. Scheible (1998), Minimum and Maximum Variance Analysis,
- ISSI Scientific Reports Series, 1, 185–220.
- Sorathia, K. A., V. G. Merkin, A. Y. Ukhorskiy, B. H. Mauk, and D. G. Sibeck (2017),
- Energetic particle loss through the magnetopause: A combined global mhd and test-
- particle study, Journal of Geophysical Research: Space Physics, 122(9), 9329–9343, doi:
- 10.1002/2017JA024268.
- Swift, D. W. (1995), Use of a hybrid code to model the Earth's magnetosphere, *Geophysi*-
- cal Research Letters, 22, 311–314, doi:10.1029/94GL03082.
- Swift, D. W. (1996), Use of a Hybrid Code for Global-Scale Plasma Simulation, Journal
- of Computational Physics, 126, 109–121, doi:10.1006/jcph.1996.0124.
- Terasawa, T., M. Fujimoto, H. Karimabadi, and N. Omidi (1992), Anomalous ion mixing
- within a kelvin-helmholtz vortex in a collisionless plasma, *Phys. Rev. Lett.*, 68, 2778–
- 675 2781, doi:10.1103/PhysRevLett.68.2778.
- Thomas, V. A., and D. Winske (1993), Kinetic simulations of the kelvin-helmholtz insta-
- bility at the magnetopause, Journal of Geophysical Research: Space Physics, 98(A7),

- 678 11,425–11,438, doi:10.1029/93JA00604.
- Wang, L., A. H. Hakim, A. Bhattacharjee, and K. Germaschewski (2015), Comparison of
- multi-fluid moment models with particle-in-cell simulations of collisionless magnetic
- reconnection, *Physics of Plasmas*, 22(1), 012,108, doi:10.1063/1.4906063.
- Wing, S., J. R. Johnson, C. C. Chaston, M. Echim, C. P. Escoubet, B. Lavraud, C. Lemon,
- K. Nykyri, A. Otto, J. Raeder, and C.-P. Wang (2014), Review of solar wind entry
- into and transport within the plasma sheet, Space Science Reviews, 184(1), 33–86, doi:
- 10.1007/s11214-014-0108-9.
- Yee, K. (1966), Numerical solution of inital boundary value problems involving maxwell's
- equations in isotropic media, IEEE Transactions on Antennas and Propagation, 14, 302-
- 307, doi:10.1109/TAP.1966.1138693.